Development of High-Efficient Asphalt Pavement Modeling Software for Digital Twin of Road Infrastructure

Kairen Shen and Hao Wang[*]

Department of Civil and Environmental Engineering, School of Engineering, Rutgers, The State University of New Jersey, New Brunswick, USA, 08854 (*Corresponding author, hwang.cee@rutgers.edu)

Abstract

To develop digital twin (DT) of road infrastructure, one critical element is computation of pavement responses (strains, stresses, and deflections) under traffic and environmental loading. This study aims to develop high-efficient asphalt pavement modeling software based on semi-analytical finite element method (SAFEM) for DT application. The algorithms address important aspects in vehicle-tire-pavement interaction modeling, such as dynamic vehicular loading, three-dimensional (3-D) non-uniform tire contact stress, viscoelastic behavior of asphalt material, and interface bonding condition. The simulation accuracy is verified by comparison with full-scale test and field measurements, and the relative differences are around 5% to 20%. Techniques including optimized discrete Fourier transform, parallel computing, graphics processing unit (GPU) acceleration, and sparse matrices are implemented for computation efficiency. As compared to the traditional 3-D FEM, SAFEM shows significant savings in computation time and storage usage. The high efficiency and accuracy make the software full of potential to be applied for DT of roadway infrastructure.

Keywords: Roadway infrastructure; Digital twin; Pavement responses; Semi-analytical finite element method; Software development

1 Introduction

Digital twin (DT), emerging as a synthesis of information technology and analysis modeling, is heralding an industrial revolution across various sectors, including the roadway infrastructure [1]. The DT of roadway infrastructure can be seen as an integrated multi-physical and multi-scale simulation, where real-world data mirror the virtual twins along the whole life cycle [2]. The virtual twin not only enables precise simulation of the real world but also facilitates the acquisition of data that is otherwise challenging to obtain in the physical world. This innovation offers precise prediction and proactive decision-making in road maintenance and repair based on the implementation of real-time cyber-physical data updates [3].

The schematic diagram of DT for roadway infrastructure is shown in Figure 1, including structural monitoring, data acquisition and storage, analysis model, and visualization [4]. Structural monitoring involves sensors and monitoring technologies on the real-world infrastructure to gather in-situ conditions continuously [5]. These data are stored and processed for further analysis. Analysis models, as the system core, simulate the infrastructure behavior in a real environment efficiently. Analysis models of DT can be categorized into physics-based and data-driven types [3]. Pure physical models are detailed and accurate but computationally demanding, hindering real-time simulations. Data-driven models are relatively efficient, but they rely on specific input-output data and are limited to available training databases, not encompassing the complete picture [6]. The simulated results are transformed into virtual twins with visualization functions. Actionable intelligence finally provides predictive insights for the decision-making process of infrastructure maintenance and repair. It is critical to highlight that the above bidirectional information flow is not one-time occurrence but a continuous and iterative cycle that evolves based on constantly updated information from sensors and analysis results. This continuous loop of data update, model analysis, and decision-making underscores the advanced capabilities of DT over traditional static simulation models, embodying a more proactive, precise, and adaptive approach to road infrastructure management [7].
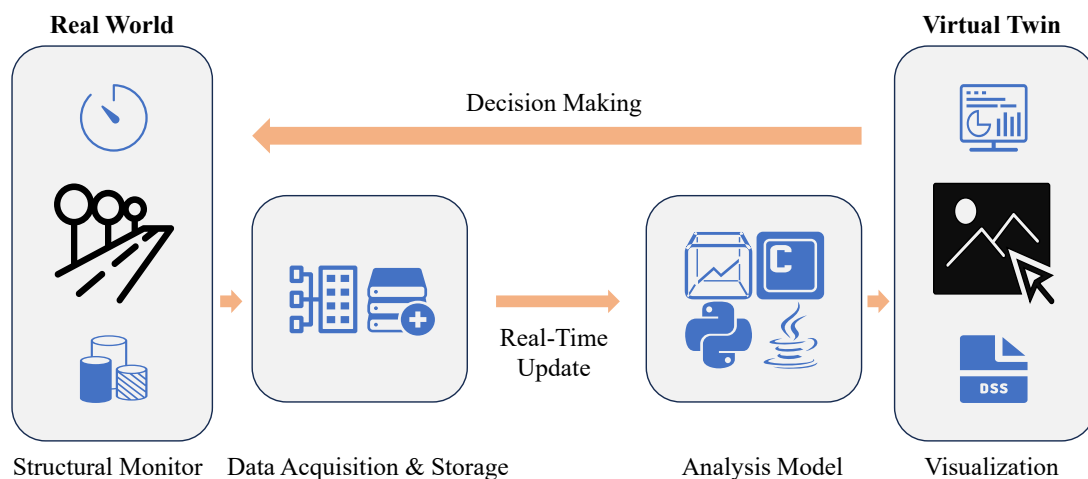

2

Figure 1. Schematic diagram of DT for road infrastructure.

In flexible pavement engineering, response indicators such as stress and strain serve as vital links connecting material experiments, pavement response, and long-term performance . The majority of asphalt mixture experiments related to material performance are conducted under controlled strain or stress conditions, with the other parameter serving as the measurement indicator [8]. Furthermore, whether utilizing physical models, empirical mechanical models, or data-driven models, the pavement responses induced by vehicles are critical indicators for predicting the evolution of long-term pavement performance (cracking and rutting) [9,10]. Therefore, one critical analysis model of the road infrastructure DT is computation of pavement responses (strains, stresses, and deflections) under traffic loading and environmental conditions. Physical models for pavement response prediction have continued to evolve for nearly a century. In view of the space dimensions, standard models include the multi-layered elastic method (MLEM) [11], two-dimensional (2-D) plate strain finite element method (FEM) [12], and three-dimensional (3-D) FEM [13]. Indeed, the MLEM can be conceptualized as one-dimensional (1-D) FEM considering degrees of freedom. The time complexity of these three models increases exponentially, with the corresponding enhancement in simulation complexity and accuracy. The specific runtime of models varies with material and structural settings as well as computer performance, but the differences among models with different dimensions are significant. The computation time for 1-D models is very short and often negligible, making them particularly suitable for the preliminary design stage [14]. 2-D FEM usually requires several tens of seconds to compute [15], while 3-D FEM would cost several hours, especially for nonlinear materials [16]. However, 1-D and 2-D FEM cannot account for moving loads of traffic loading and slab joints in concrete pavements [17]. Although the 3-D FEM is versatile for various loading configurations and boundary conditions [16], it does not fulfill the efficiency criteria essential for real-time updates in DT applications.

Given the general uniformity of pavement cross-sections along the longitudinal direction, the extensive longitudinal modeling in 3-D FEM might be unnecessarily detailed. However, the 3-D representation of vehicle loading is an essential factor that must be considered. In this context, the semi-analytical finite element method (SAFEM) could offer a viable solution [18]. This method conducts meshing in cross-section and substitutes meshing with the interpolation of Fourier series along the longitudinal direction to simulate loading distribution [19]. In this way, a 3-D FEM is transformed into a series of 2-D FEM under each Fourier series, significantly enhancing the computing efficiency [18,20,21]. SAFEM has been applied in a wide range of pavement modeling scenarios, from static elastic analysis to dynamic viscoelastic analysis [17,18,22–24].

Given the high accuracy requirements of DT, it remains necessary to simulate realistic vehicle-tire-pavement interaction in SAFEM. Traffic loading is critical for pavement response and damage, but it is usually assumed as constant over the service

3

103 life of pavement [25]. However, recent studies have indicated that dynamic loading
104 with random amplitudes induced by pavement surface roughness would generate
105 noticeable variations in pavement responses [23, 24]. Since the DT simulates the whole
106 lifecycle of pavement with evolution of pavement surface roughness, dynamic loading
107 is an inescapable factor to be considered. Besides, previous studies have simulated tire-
108 pavement contact stresses as a uniform distribution within a rectangular or circular area,
109 although non-uniform contact stress distribution exists in the tire-pavement interface
110 [27]. This simplification is reasonable for calculating responses at a location far away
111 from the loading while difficult to capture the near-surface stress state of pavement that
112 is responsible for top-down cracking [26].

113 The structure monitoring component in DT will provide the real-time
114 environmental situation, such as temperature, precipitation, solar radiation, etc. Since
115 pavement material properties are environment-dependent, the relationship between
116 material property and environmental parameters should be considered in the physical
117 model [9]. For flexible pavement, asphalt mixture is viscoelastic material, and thus its
118 mechanical response varies significantly depending on temperature and vehicle speed
119 [27]. Thus, material viscoelasticity needs to be captured in physical modeling of
120 flexible pavement responses and damage. Besides, flexible pavement is a typical multi-
121 layer system, and thus the interface behavior influences mechanical responses of layers
122 [30]. For instance, the tensile strain at the bottom of asphalt surface layer might
123 transform from compression to tension as the bonding to the lower asphalt layer is lost
124 due to construction deficiency or moisture intrusion [31]. The accurate characterization
125 of interlayer conditions becomes vital for simulation precision in SAFEM.

126 While the computational algorithms in SAFEM need to fulfill the functionality of
127 simulation with high accuracy, it is also crucial to meet the efficiency requirements for
128 DT applications. There are two key strategies to enhance computational efficiency [32].
129 The first involves a trade-off between space and time complexity, exemplified by
130 parallel computing, which speeds up tasks by distributing computation across multiple
131 processors [33]. The second focuses on direct optimization of algorithms, such as GPU
132 acceleration, to significantly improve processing speed for large-scale data and
133 complex mathematical operations [34]. The bulk of computing in FEM predominantly
134 arises from solving equilibrium equations involving extensive matrix operations. For
135 example, the 2-D FEM under each Fourier series in the SAFEM is independent, which
136 can be solved in parallel [18]. Moreover, the parallel process could be further enhanced
137 by combining efficient algorithms, especially dynamic programming, sparse matrix,
138 and GPU acceleration. Therefore, an efficient simulation software can be made using
139 SAFEM for DT applications.
140

2 Objective and Scope

142 This study aims to develop high-efficient asphalt pavement modeling software based
143 on SAFEM for response calculation, serving as the most critical analysis model in DT
144 application. The algorithm functions address the most important aspects in vehicle-tire-

145 pavement interaction modeling, such as dynamic vehicular loading, three-dimensional
146 non-uniform tire contact stress, viscoelastic behavior of asphalt materials, and interface
147 bonding conditions. The software efficiency is ensured by a series of computer
148 algorithms, including optimized discrete Fourier transform, parallel computing, GPU
149 acceleration, and sparse matrices. The efficiency and accuracy of the developed
150 software are verified by comparisons with 3D-FEM and field instrumentation
151 measurements. The software is developed with a packaged version with a Graphic User
152 Interface (GUI) and a command-line version.
153

154 **3 Software Architecture Design**
155 Software design is generally a two-step process, where architectural design first
156 describes the software organization components, and detailed design describes the
157 desired behavior of these components [35]. Following this logic, the architectural
158 design will be presented first, and then the detailed function and algorithm will be
159 expanded.
160   Generally, programming principles can be divided into object-oriented
161 programming (OOP) and procedural programming (PP), of which fundamental units of
162 execution are class and function, respectively. PP emphasizes the sequential execution
163 of functions, while OOP enables classes to operate independently, avoiding the
164 cascading effects common in function-based approaches [35]. In other words, OOP
165 simplifies complex systems into manageable components, promotes code reuse, and
166 facilitates function expansion. To facilitate the software expansion for future research,
167 OOP is employed in this study to develop the software SAFEM_DT, and each colored
168 block in Figure 2 corresponds to a class.
169   The nature behind SAFEM is transforming 3-D equilibrium equations of FEM into
170 a series of 2-D equations in Fourier series domains, while the other computation
171 processes are like traditional FEM. As shown in Figure 2, the software has been
172 deconstructed into three main procedures: pre-processing, computing core, and post-
173 processing. The pre-processing achieves loading transform, geometry development,
174 meshing, material assembly, temperature field, boundary and interface configuration,
175 and analysis step setting. This procedure mainly completes preparation of partial
176 differential equations for vehicle-pavement interaction. The computing core will solve
177 these equations in an iteration form of dynamic analysis. This procedure takes up most
178 software workloads, of which algorithm optimization is essential for enhancing
179 efficiency. The post-processing mainly achieves visualization of pavement responses in
180 time and spatial domains, where Fourier inversion transform will be conducted to
181 transform results from Fourier series domains to 3-D space domain.
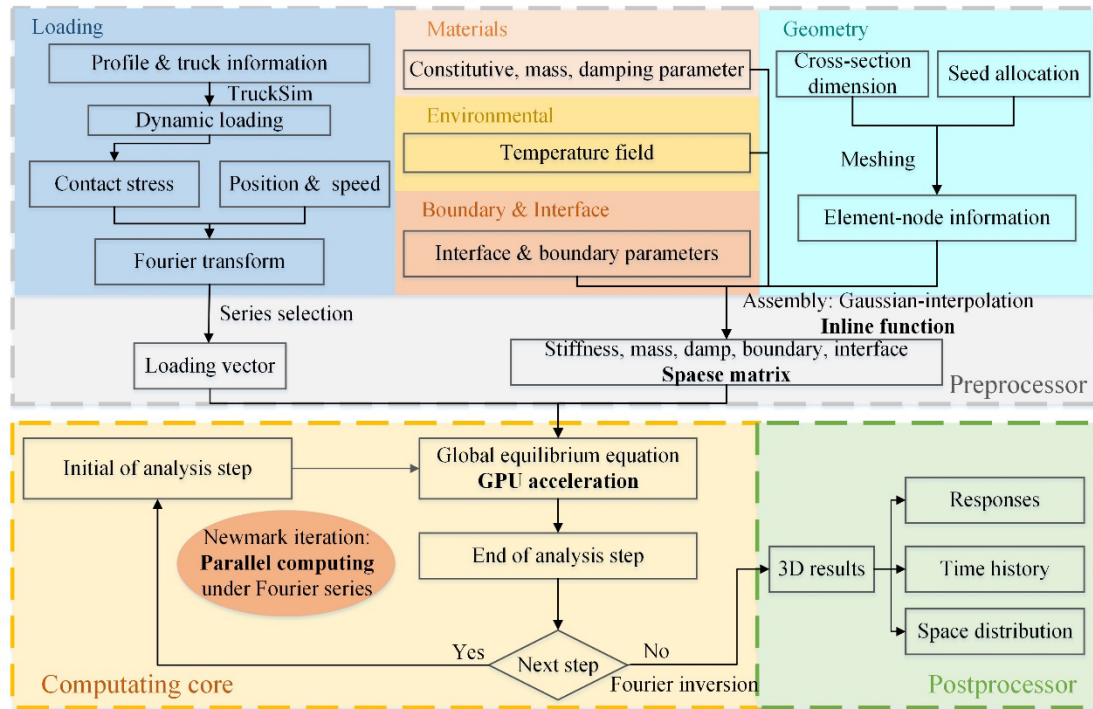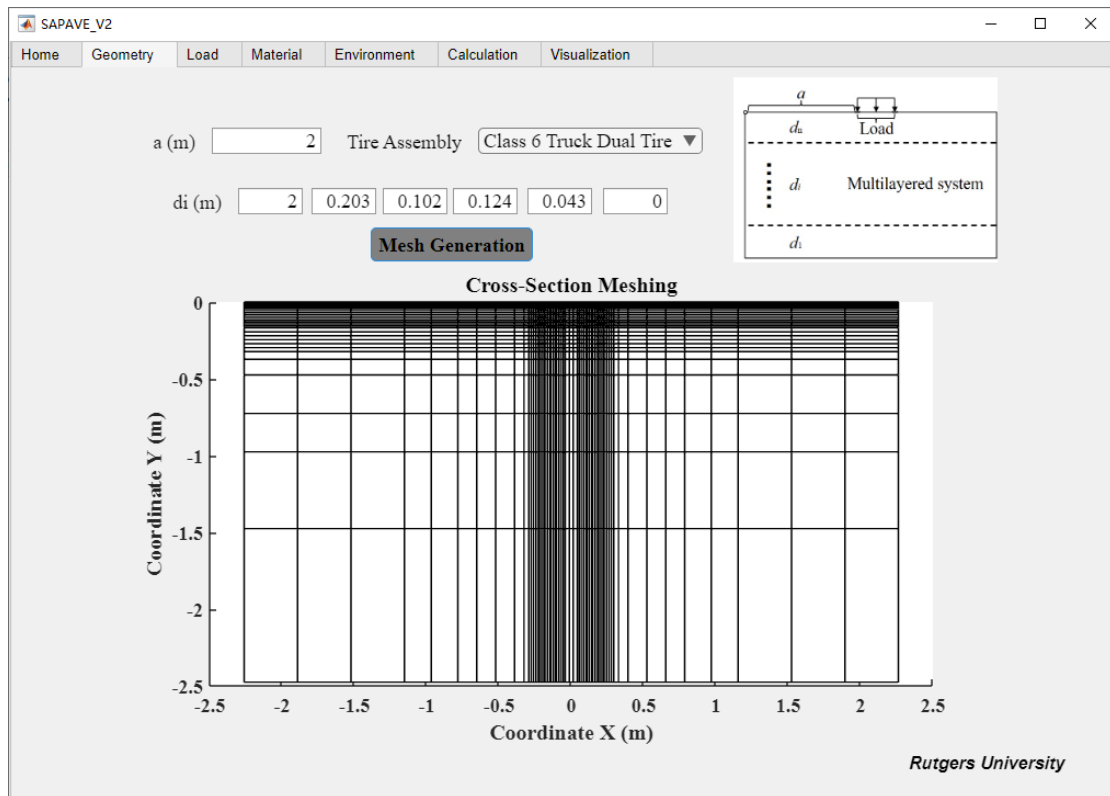182

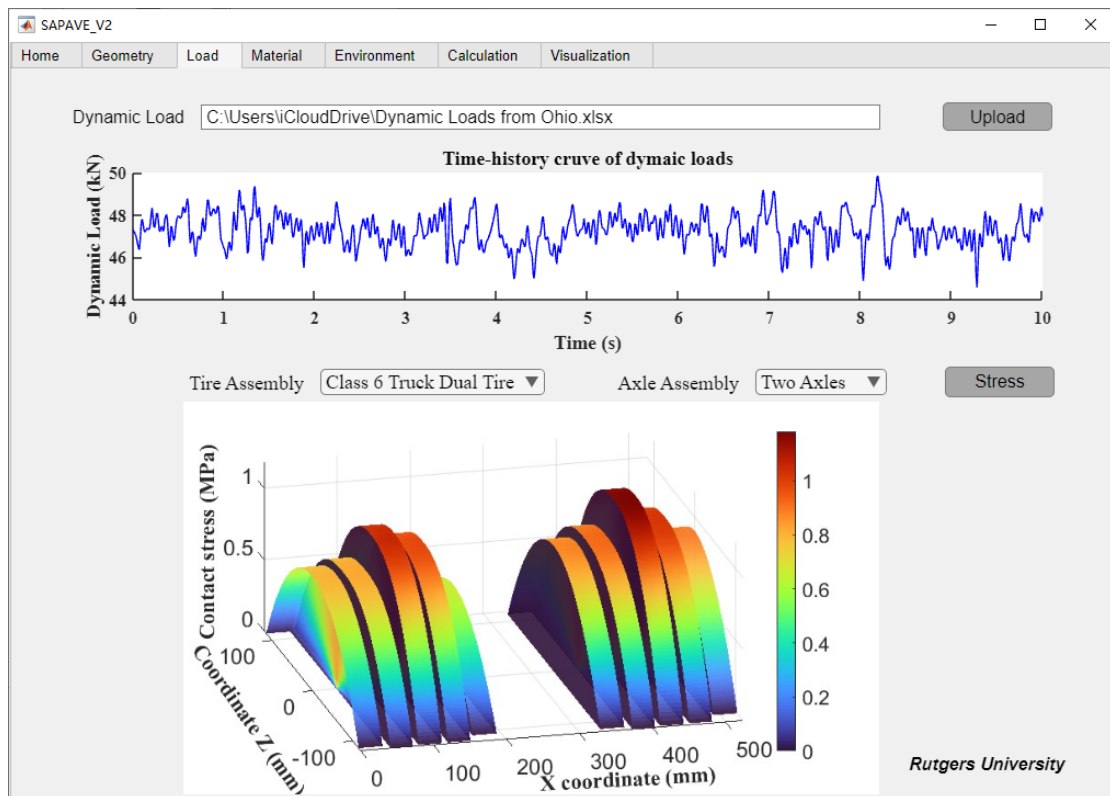Figure 2. Architecture design of SAFEM_DT software.

A GUI is developed based on the software architecture, of which several critical interfaces about geometry, loading, material, and environment modules are presented in Figure 3. The geometry module will automatically generate the meshing in cross-section based on pavement thickness and width inputs and the configuration of axle and tire assembly. The loading module will input the dynamic loading, tire, and axle configurations, which will be utilized to conduct the Fourier transform. The material and environment modules will input the required material and temperature parameters.

6

194
195   (a)

196
197   (b)

198

199   (c)

200

201   (d)

202   Figure 3. Software GUIs for (a) Geometry, (b) Loading, (c) Material, and (d)

203   Environment modules.

204

4 Computational Algorithms and Functions

4.1 Global Equilibrium of SAFEM

SAFEM only conducts a 2-D meshing in cross-section and utilizes Fourier series to replace meshing along the longitudinal direction. Then, the representation of all variables in longitudinal space domain is transformed into Fourier series domain. Let (x, y, z) be coordinates describing the 3-D space domain. The longitudinal direction z, along which pavement geometry and material property usually do not change, is limited to between 0 to a. Taking displacement u as an example, variables of SAFEM have the following form:

$$u(x, y, z) = \sum_{l=0}^{L} [u_{lc}(x, y) \cos(l\pi z / a) + u_{ls}(x, y) \sin(l\pi z / a)] \tag{1}$$

where, l is the number of Fourier series dimensions, and u_l is the displacement component in the corresponding Fourier domain. The variables of SAFEM are 3-D vectors corresponding to the 3-D space domain [19], which is the most notable difference from 2-D FEM.

The pavement model developed in this study is presented in Figure 4. The applied load with random amplitudes is induced by pavement roughness [13]. The asphalt layers are treated as viscoelasticity, of which constitutive model is selected as the Generalized Maxwell Model (GMM) [36]. The temperature-dependent of viscoelastic materials has been considered according to the temperature field. The other layers are treated as elasticity with damping effects, accounting for the energy consumption during the dynamic process. An artificial element simulates the interface between adjacent layers and can represent different friction conditions. Boundary conditions are assumed as supporting and absorbing for the bottom and vertical, respectively.
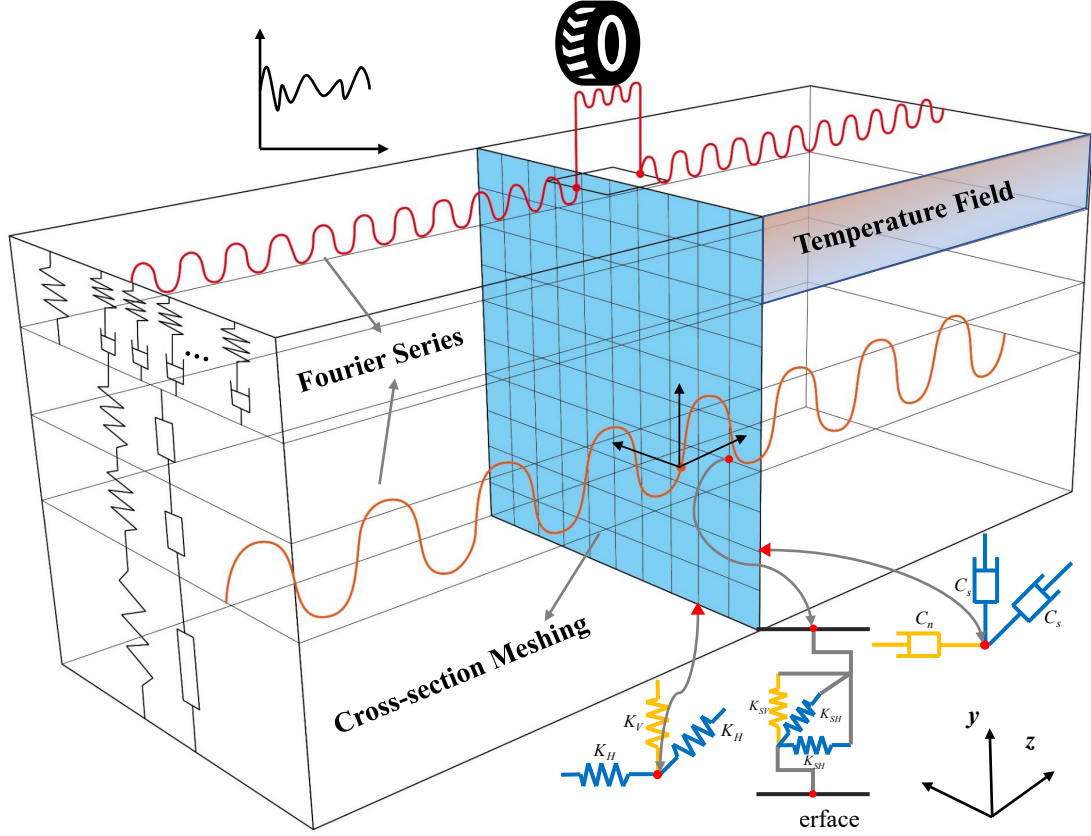
227

229   Figure 4. Schematic representation of the SAFEM for flexible pavement.

230

231   In the dynamic process, assume δW_S, δW_I, δW_D, δW_G, δW_L, δW_B, and δW_i are the

232   virtual work done by the stress, inertia, damping, gravity, loading, boundary, and

233   interface on a virtual strain $\delta\varepsilon$, respectively. These virtual works and global equilibrium

234   can be presented as follows:

$$\delta W_S = \int_\Omega [\delta\boldsymbol{\varepsilon}(t)]^T \boldsymbol{\sigma}(t)d\Omega$$

$$\delta W_I = \int_\Omega [\delta\mathbf{u}(t)]^T \rho\ddot{\mathbf{u}}(t)d\Omega$$

$$\delta W_D = \int_\Omega [\delta\mathbf{u}(t)]^T c\dot{\mathbf{u}}(t)d\Omega$$

$$\delta W_G = \int_\Omega [\delta\mathbf{u}(t)]^T \mathbf{g}d\Omega \tag{2}$$

$$\delta W_L = \int_\Gamma [\delta\mathbf{u}(t)]^T \mathbf{F}_L(t)d\Gamma$$

$$\delta W_B = \int_\Gamma [\delta\mathbf{u}(t)]^T \mathbf{F}_B(t)d\Gamma$$

$$\delta W_i = \int_\Gamma [\delta\mathbf{u}(t)]^T \mathbf{F}_i(t)d\Gamma$$

$$\delta W_S + \delta W_I + \delta W_D + \delta W_G + \delta W_L + \delta W_B + \delta W_i = 0 \tag{3}$$

235   where, $\mathbf{u}$, $\dot{\mathbf{u}}$ and $\ddot{\mathbf{u}}$ are the displacement, velocity, and acceleration vectors; ρ and c are

236   the density and damping coefficients, respectively; $\mathbf{g}$, $\mathbf{F}_L(t)$, $\mathbf{F}_B(t)$, and $\mathbf{F}_i(t)$ are the

237   gravity, loading, boundary condition, and interface functions, respectively. It can be

238   found that the virtual works of inertia and damping are related to acceleration and

239   velocity, respectively, while the others are related to displacement.

4.2 Geometry and Meshing

Geometry development is the beginning of FEM, where 3-D geometry of different layers is input according to actual structures. Meshing seed is allocated by a gradient guideline, which is dense to thin with the distance from the loading area. The seed allocation is also precisely adjusted to tire rib and groove positions.

Meshing adopts the Four-node isoparametric rectangle element, of which Langrage shape function N_i in local coordinates (ξ, η) is as follows:

$$N_i(\xi, \eta) = \frac{1}{4}(1 \pm \xi)(1 \pm \eta) \ \text{with} \ i = 1, 2, 3, 4 \tag{4}$$

The combined shape function of a SAFEM element in the Fourier dimension l is as follows:

$$\mathbf{N}^l = [\mathbf{N}_1 \quad \mathbf{N}_2 \quad \mathbf{N}_3 \quad \mathbf{N}_4]$$
$$\mathbf{N}_i = N_i * [\sin(l\pi z/a) + \cos(l\pi z/a)] * eye(3) \tag{5}$$

The corresponding strain-displacement matrix $\mathbf{B}$ is as follows:

$$\mathbf{B}^l = [\mathbf{B}_1 \quad \mathbf{B}_2 \quad \mathbf{B}_3 \quad \mathbf{B}_4]$$

$$\mathbf{B}_i = \begin{bmatrix} \partial N_i/\partial x \, (s+c) & 0 & 0 \\ 0 & \partial N_i/\partial y \, (s+c) & 0 \\ 0 & 0 & l\pi/a \, N_i(c-s) \\ \partial N_i/\partial y \, (s+c) & \partial N_i/\partial x \, (s+c) & 0 \\ 0 & l\pi/a \, N_i(c-s) & \partial N_i/\partial y \, (s+c) \\ l\pi/a \, N_i(c-s) & 0 & \partial N_i/\partial x \, (s+c) \end{bmatrix} \ \text{with} \ \begin{matrix} s = \sin(l\pi z/a) \\ c = \cos(l\pi z/a) \end{matrix} \tag{6}$$

4.3 Dynamic Loading and Tire-Pavement Contact Stresses

Vehicle loading is the most critical input for pavement modeling. According to some field measurements, tire contact stress is three-direction and non-uniformly distributed on ribs separated by grooves, of which the distribution pattern is related to tire types and loading weight [37]. Recent studies have indicated that pavement roughness generates dynamic loading with random amplitudes [38], which can be inferred to change the contact stress distribution simultaneously. Therefore, the dynamic contact stress induced by pavement roughness should be simulated.

The Fourier transform of the contact stress is illustrated in Figure 5. Detailed processes can be summarized as follows:

1. Input pavement profile, i.e. the surface elevation along the longitudinal direction, and vehicle information, such as suspension parameters, weight, and speed, to obtain the location-history dynamic axle loading [39]. TruckSim, a multi-body dynamic software, was used in this study to complete the task [13], which can also be achieved by many other existing models or software.

2. The axle loading is then used to obtain the three-directional contact stresses in vertical, transverse, and longitudinal directions. An empirical regression model driven by field measurements is adopted to predict contact stress [37]. A typical dual-tire assembly and a wide base tire are included in the measurements. Since

269   the transverse stiffness of tire is significantly larger than the longitudinal, the
270   stress distribution of each rib along lateral direction is assumed to be constant
271   [40], while the distribution along driving direction can be predicted as follows:

$$q(\epsilon) = \alpha \frac{P}{l_t}\left(1+\frac{1}{2n}\right)(1-\epsilon^{2n})$$

$$\text{with} \quad l_t = d_1 + d_2 P$$

$$\epsilon = \frac{2z}{l_t}$$

$$n = k_1 + k_2\frac{P}{10^3} + k_3\frac{S}{10^3}$$

$$\alpha = c_1 + c_2\frac{P}{10^3} + c_3\frac{S}{10^3} + c_4\left(\frac{P}{10^3}\right)^2 + c_5\left(\frac{S}{10^3}\right)^2$$

(7)

272   where, P is the applied loading, S is the tire inflation pressure, l_t is the contact
273   length, ϵ is the normalized distance along the contact length, z is the coordinate
274   value from - l_t /2 to l_t /2, and d_i, k_i, and c_i are regression coefficients depending
275   on tire types, rib numbers, and stress direction [37].

276   3.   Conduct discrete Fourier transform (DFT) for stress on each rib individually to
277   transfer the distribution function in longitudinal space domain to Fourier series
278   domain. Since a higher weight coefficient of Fourier series corresponds to more
279   contributions to the inverse discrete Fourier transform (IDFT), a limit series
280   search is operated to ensure the minimum selected series meets the fitting
281   requirement. The series selection reduces the following computing amount
282   because the number of series corresponds to that of 2-D FEM. The transformed
283   loading function is as follows:

$$\mathbf{P}(x,y,z,t) = \sum_{\text{selected } l} [\mathbf{P}_{ls}(x,y,t)\sin\frac{l\pi z}{a} + \mathbf{P}_{lc}(x,y,t)\cos\frac{l\pi z}{a}]$$

(8)

284   4.   The Fourier series of different ribs are finally combined according to the Fourier
285   series number l. The loading allocation in coordinates x and y is based on the
286   rib position in the cross-section.
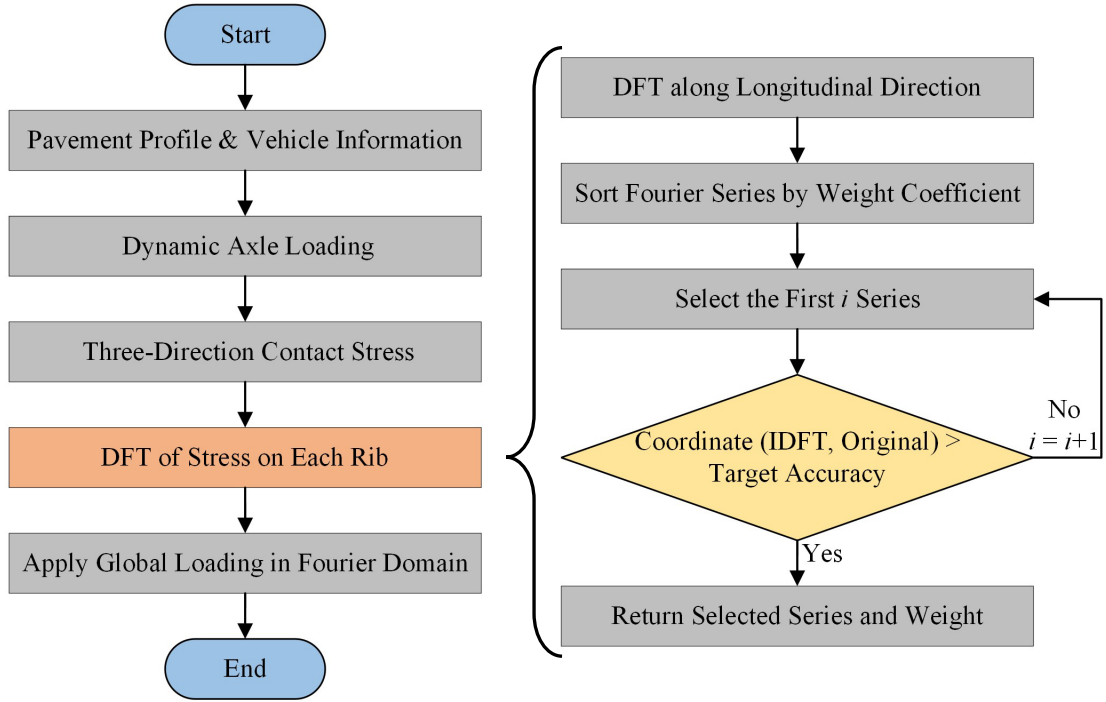
287

288
289   Figure 5. Fourier transform of tire contact stress induced by pavement roughness.
290

291   The above process for the vertical contact stress of the eighth rib shown in
292   Figure 3(b) can be illustrated in Figure 6. For a 10-meter longitudinal distribution with
293   an interval of 0.02 m, 1002 Fourier series will be obtained from a DFT. Based on a
294   selection of Fourier series with higher weights shown in Figure 6(a), a total of 54 series
295   is selected to simulate the loading distribution with a cross-correlation of 0.98 shown
296   in Figure 6(b), where the cross-correlation is a measure of two-series similarity and
297   usually representing good similarity if it is larger than 0.9. Only 3% of Fourier series
298   are selected to achieve a 98% fitting accuracy [22]. Since the computation amount of
299   SAFEM is proportional to the number of Fourier series, the treatment of series selection
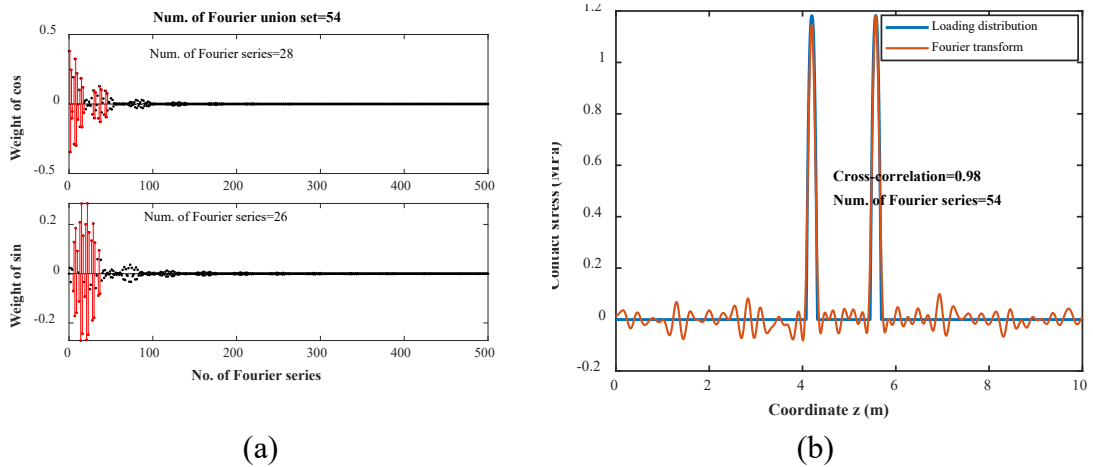300   will increase computing efficiency by 20 times significantly.
301

                        (a)   (b)
302   Figure 6. (a) Fourier series selection and (b) fitting of contact stress distribution.

13

303 *4.4 Material Assembly and Temperature Field*

304 Material assembly of an element in SAFEM generally consists of stiffness $\mathbf{K}$, mass $\mathbf{M}$,

305 and damping $\mathbf{C}$ matrices as follows:

$$\mathbf{K}^e = \int_\Omega \mathbf{B}^T \mathbf{D} \mathbf{B} d\Omega = (\mathbf{K}^{lm})_{L \times L}$$

$$\mathbf{M}^e = \int_\Omega \mathbf{N}^T \rho \mathbf{N} d\Omega = (\mathbf{M}^{lm})_{L \times L} \tag{9}$$

$$\mathbf{C}^e = \int_\Omega \mathbf{N}^T c \mathbf{N} d\Omega = (\mathbf{C}^{lm})_{L \times L}$$

306 where, l and m are the Fourier domain numbers. Besides, the following integrations are

307 contained in matrices:

$$I_1 = \int_0^a \sin\frac{l\pi z}{a} \sin\frac{m\pi z}{a} dz$$

$$I_2 = \int_0^a \cos\frac{l\pi z}{a} \cos\frac{m\pi z}{a} dz$$

$$I_3 = \int_0^a \sin\frac{l\pi z}{a} \cos\frac{m\pi z}{a} dz \tag{10}$$

$$I_1 = I_2 = \begin{cases} \frac{1}{2}a, l = m \\ 0, \quad l \neq m \end{cases} \quad \text{and} \quad I_3 = 0$$

308 Thus, the 3-D matrices are transformed to block diagonal matrices as follows:

$$\mathbf{K}^e = diag(\mathbf{K}^{ll})_{\text{selected } l}$$

$$\mathbf{M}^e = diag(\mathbf{M}^{ll})_{\text{selected } l} \tag{11}$$

$$\mathbf{C}^e = diag(\mathbf{C}^{ll})_{\text{selected } l}$$

309 The transform is also the principle that the SAFEM replaces 3-D FEM with a series

310 of independent 2-D FEM in Fourier series domains.

311 Four-Gauss-Point interpolation in local coordinates is utilized to solve the

312 matrix integrations, and all element integrations are integrated into global coordinates

313 by the Jacobian transform matrix $\mathbf{J}$ and the element-node relationship [18]. Take the

314 stiffness matrix as an example shown as follows:

$$\mathbf{K}^{ll} = a/2 \int_A \overline{\mathbf{B}}^T \mathbf{D} \overline{\mathbf{B}} dxdy = \sum_{i=1}^4 a/2 \overline{\mathbf{B}}^T \mathbf{D} \overline{\mathbf{B}} W_i \det \mathbf{J} \tag{12}$$

315 where, W_i is the unit weight of Gauss points, taken as one in this study.

316 Asphalt mixture of flexible pavement is a typical time- and temperature-dependent

317 material, of which constitutive model GMM transformed into a Prony series form is as

318 follows [28]:

$$E(t) = E_\infty + \sum_{i=1}^n E_i e^{-t/\rho_i}$$

$$\text{with} \quad E(t_r, T) = E(t, T_{ref})$$

$$t_r = t / a_T \tag{13}$$

$$\log(a_T) = -\frac{C_1(T - T_{ref})}{C_2 + (T - T_{ref})}$$

319   where, E_∞, E_i, and ρ_i are the GMM parameters; T and T_{ref} are targeted and reference
320   temperatures, respectively; t_r is reduced relaxation time; a_T is the temperature shift
321   factor expressed by Williams–Landel–Ferry (WLF) equation with empirical constants
322   C_1 and C_2 [41].

323   The material assembly combined with temperature field can be illustrated in
324   Figure 7. First, the temperature profile of cross-section is obtained from field
325   measurement or prediction methods to supply the coordinate-temperature relationship.
326   Then, modify the reduced relaxation time at Gauss point based on the relationship. Next,
327   integrate the element matrix in local coordinates and assemble entire matrix in global
328   coordinates. Besides, local or inline functions are utilized to form local matrices in the
329   function of global matrices assembly, which will save much time on function calls. The
330   global matrices are stored in a sparse form, which ignores the zero element. It will save
331   much memory usage and enhance computing efficiency.
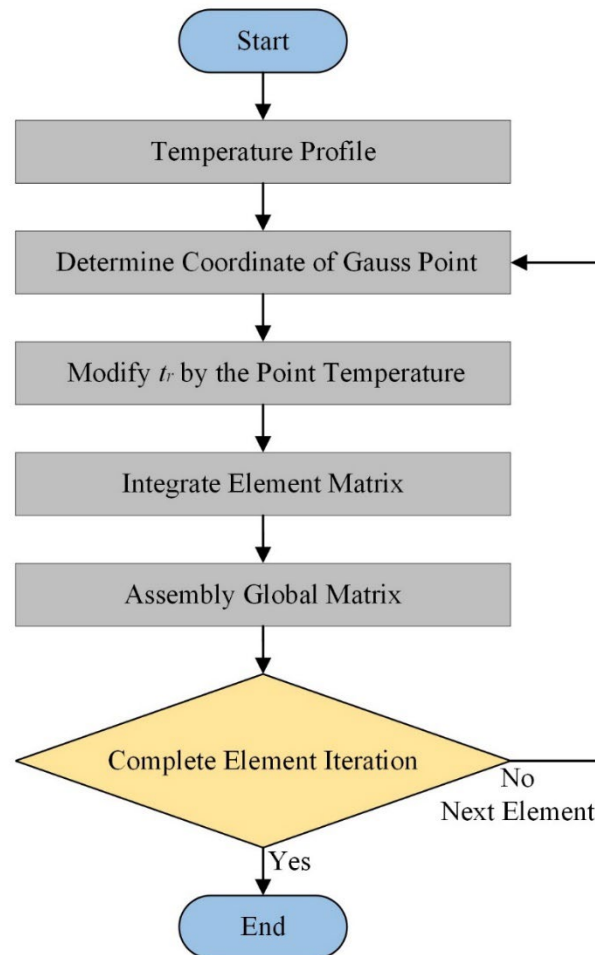332

333
334   Figure 7. Viscoelastic material assembly with temperature field.
335
336   Unlike the instantaneity of elastic stress, viscoelastic stress depends on the
337   whole strain history, which can be expressed as a convolution form as follows:

$$\boldsymbol{\sigma}(t)=\int_0^t E(t-\tau)\frac{\partial \boldsymbol{\varepsilon}(t)}{\partial \tau}d\tau \tag{14}$$

338 which can be expressed as the following iteration form in the dynamic analysis:

$$\boldsymbol{\sigma}_{n+1} = \boldsymbol{\sigma}_n + \int_{t-\Delta t}^t E(t-\tau)\frac{\partial \boldsymbol{\varepsilon}}{\partial \tau}d\tau + \sum_{i=1}^n E_i(e^{-\Delta t/\rho_i}-1)\mathbf{P}_n^i$$

$$\text{with } \mathbf{P}_n^i = \int_0^{t-\Delta t} e^{-(t-\Delta t-\tau)/\rho_i}\frac{\partial \boldsymbol{\varepsilon}}{\partial \tau}d\tau \tag{15}$$

339 Trapezoidal integral method can be used to solve the partial derivative of strain as
340 follows:

$$\int_{t-\Delta t}^t E(t-\tau)\frac{\partial \boldsymbol{\varepsilon}}{\partial \tau}d\tau \approx \int_{t-\Delta t}^t E(t-\tau)d\tau \frac{\boldsymbol{\varepsilon}_{n+1}-\boldsymbol{\varepsilon}_n}{\Delta t}$$

$$\mathbf{P}_n^i \approx e^{-\Delta t/T_i}\mathbf{P}_{n-1}^i + \int_{t-2\Delta t}^{t-\Delta t} e^{-(t-\Delta t-\tau)/\rho_i}d\tau \frac{\boldsymbol{\varepsilon}_n-\boldsymbol{\varepsilon}_{n-1}}{\Delta t} \tag{16}$$

341 Newton-Cotes formula can be further applied to solve the convolution as follows:

$$Cotes(E)=\int_{t-\Delta t}^t E(t-\tau)d\tau$$

$$=\frac{1}{90}[90E_\infty + \sum_{i=1}^n E_i(7+32e^{-0.25\Delta t/\rho_i}+12e^{-0.5\Delta t/\rho_i}+32e^{-0.75\Delta t/\rho_i}+7e^{-\Delta t/\rho_i})]$$

$$Cotes(e) = \int_{t-2\Delta t}^{t-\Delta t} e^{-(t-\Delta t-\tau)/\rho_i}d\tau$$

$$=\frac{1}{90}(7+32e^{-0.25\Delta t/\rho_i}+12e^{-0.5\Delta t/\rho_i}+32e^{-0.75\Delta t/\rho_i}+7e^{-\Delta t/\rho_i}) \tag{17}$$

342 Therefore, the viscoelastic stress can be solved as follows:

$$\boldsymbol{\sigma}_{n+1} \approx \boldsymbol{\sigma}_n + Cotes(E)\mathbf{B}\frac{\mathbf{u}_{n+1}-\mathbf{u}_n}{\Delta t} + \sum_{i=1}^n E_i(e^{-\Delta t/\rho_i}-1)\mathbf{P}_n^i$$

$$=\mathbf{K}_1\mathbf{B}\mathbf{u}_{n+1}+\mathbf{K}_2\mathbf{B}\mathbf{u}_{1\sim n} \tag{18}$$

343 **4.5 Interface and Boundary Element**
344 Interface conditions between adjacent pavement layers generally can be classified into
345 three types: full-bonded, frictionally sliding, and frictionless [27]. The favorable
346 interface between nearly simultaneously layered asphalt layers is full-bounded or strong
347 bonded with high shear strength since aggregate embedding and asphalt bonding
348 reinforce the interlayer under high-temperature rolling construction, while the interface
349 between asphalt layer with existing asphalt or base layer is usually frictionally sliding
350 [42]. Frictionless interface or interface with low shear strength between asphalt layer
351 and base is strongly avoided in pavement structures because it can increase the near-
352 surface shear strain and quickly induce shoving or lump diseases [43]. The interface
353 between other layers, such as cement-treated base, aggregate base, or subgrade, is
354 usually treated as frictionally sliding. Besides, interface conditions significantly affect
355 pavement responses. For example, in a typical composite pavement with an asphalt
356 layer overlaying cement concrete layers, the strain at the bottom of the asphalt layer
357 changed from tensile to compressed when the interface changed from frictionless to
358 full-bonded [31].

359   Direct shear experiments are widely used for pavement structures to determine
360 interface conditions. The test will record the time history of relative displacement with
361 applied loads, where an approximate linear relationship occurs at the loading phase [30].
362 The linear relationship means the interface condition can be represented by three-
363 direction linear stiffness in the non-destructive phase. Transverse and longitudinal
364 stiffnesses are transformed from the test results, while the vertical is set significantly
365 larger to prevent unreasonable element penetration or separation. Based on a
366 comprehensive direct shear experiment of numerous asphalt specimens, the horizontal
367 stiffness of interface between asphalt layer with existing layers is around 0.1 to 0.3
368 MPa/mm [44]. The vertical stiffness can be set as 100 MPa/mm by a simulation
369 verification to prevent element penetration or separation [31]. An artificial two-node
370 element without weight or volume is set as the interface element to characterize the
371 experiment results. The whole process is illustrated in Figure 8.
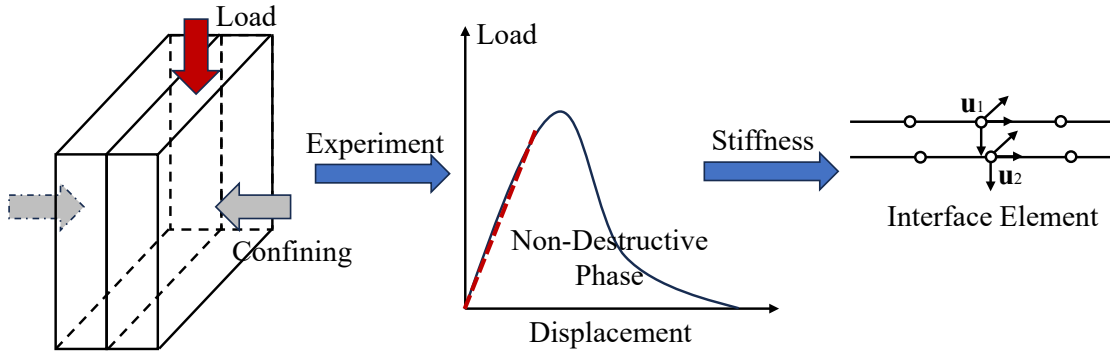372

373
374   Figure 8. Development of interface element from experiment results.
375
376   The interface element can be viewed as an energy storage device. The virtual work
377 δW_i done by an interface element at a virtual displacement $\delta\mathbf{u}$ can be calculated as
378 follows:

$$
\begin{aligned}
\delta W &= \int_{\Gamma} (\delta\mathbf{u}_1 - \delta\mathbf{u}_2)^T \mathbf{F}(t)d\Gamma \\
&= \int_{\Gamma} (\delta\mathbf{u}_1 - \delta\mathbf{u}_2)^T \mathbf{k}(\mathbf{u}_1 - \mathbf{u}_2)d\Gamma \\
&= \delta\mathbf{u}^T \int_{\Gamma}
\begin{Bmatrix} k_t \\ k_t \\ k_v \\ k_v \\ k_l \\ k_l \end{Bmatrix}^T
\begin{bmatrix}
1 & -1 & & & & \\
-1 & 1 & & & & \\
& & 1 & -1 & & \\
& & -1 & 1 & & \\
& & & & 1 & -1 \\
& & & & -1 & 1
\end{bmatrix}
\begin{Bmatrix} u_1 \\ u_2 \\ v_1 \\ v_2 \\ w_1 \\ w_2 \end{Bmatrix} d\Gamma
\end{aligned}
\tag{19}
$$

379 where, $\mathbf{u}_1$ and $\mathbf{u}_2$ are the displacement vectors of the adjacent nodes; k_t, k_v, and k_l are
380 the transverse, vertical, and longitudinal stiffnesses, respectively.
381   Three-direction spring element is applied at the model bottom to simulate the
382 subgrade supporting effect [18]. The horizontal and vertical stiffness K_H and K_V are

17

383   calculated as follows:

$$K_H = \frac{4.6E \sqrt{D_S/2}}{(1+v)(2-v)}$$

$$K_V = \frac{2.35E \sqrt{D_S/2}}{(1-v^2)}$$

$$(20)$$

384   where, D_S is the contact area.

385   Absorbing element is utilized at the vertical boundary to reduce the interference

386   of reflected waves. The principle is applying traction to make boundary velocity zero

387   as follows:

$$T_n = \rho \sqrt{\frac{E(1-v)}{(1+v)(1-2v)\rho}} \dot{u}_n$$

$$T_s = \rho \sqrt{\frac{E}{2(1+v)\rho}} \dot{u}_s$$

$$(21)$$

388   where, T_n and T_s are the normal and shear tractions, respectively; $\dot{u}_n$ and $\dot{u}_s$ are the

389   normal and tangential velocities, respectively.

390   *4.6 Dynamic Analysis Iteration*

391   The equilibrium equation under the *l*th dimension of Fourier series domain is shown as

392   follows:

$$\mathbf{K}_e^{ll}\mathbf{u}_n^l + \mathbf{K}_{ve}^{ll}\mathbf{u}_{0\sim n}^l + \mathbf{C}^{ll}\dot{\mathbf{u}}_n^l + \mathbf{M}^{ll}\ddot{\mathbf{u}}_n^l + \mathbf{F}_G^l + \mathbf{F}_L^l + \mathbf{K}_{Bb}^{ll}\mathbf{u}_n^l + \mathbf{C}_{Bv}^{ll}\dot{\mathbf{u}}_n^l + \mathbf{K}_i^{ll}\mathbf{u}_n^l = 0 \qquad (22)$$

393   where, products are the contributions of elastic stress, viscoelastic stress, damping,

394   inertia, gravity, loading, bottom boundary, vertical boundary, and interface in that order.

395   In order to solve the unknown displacement, the Newmark-beta method is utilized

396   to transform velocity and acceleration into forms of displacement as follows:

$$\ddot{\mathbf{u}}_n = 4/(\Delta t)^2 (\mathbf{u}_n - \mathbf{u}_{n-1}) - 4/\Delta t\, \dot{\mathbf{u}}_{n-1} - \ddot{\mathbf{u}}_{n-1}$$

$$\dot{\mathbf{u}}_n = 2/\Delta t\, (\mathbf{u}_n - \mathbf{u}_{n-1}) - \dot{\mathbf{u}}_{n-1}$$

$$(23)$$

397   where, acceleration is assumed as constant during each analytical step. Fourier

398   inversion transform can be conducted to get the displacement in 3-D space domain, and

399   all responses can be obtained according to the displacement-strain-stress relationship.

400   GPU acceleration can be applied to the dynamic iteration at qualified hardware.

401   Since the GPU kernel is good at floating-point calculation, it can significantly improve

402   efficiency of matrix operations, where matrices should be converted to single-precision

403   form for a better effect. Since the dynamic iteration under each Fourier series is

404   independent, parallel computing can allocate these independent iteration processes to

405   different kernels, which maximizes the use of CPU or GPU kernels.

406

407   **5 Software Validation and Efficiency Analysis**

408   *5.1 Accuracy Validation by Comparison with Full-scale Laboratory Test*

409   The software simulation accuracy was first verified by comparison with an accelerated

asphalt test [45–47]. The full-scale flexible pavement consisted of four layers: an asphalt surface, an unbound granular base, a subbase, and subgrade. The pavement temperatures of 25 and 45 °C were selected for the software comparison, of which pavement parameters are summarized in Table 1. Strain gauges were installed at two different depths, 6 and 30 cm, below the surface. The testing facility MLS66 with dual-tire assembly was used for the loading application, of which axle load was 50 kN, and the motion speed was 11 km/h.

Table 1. Parameters of the pavement structure layers.

Structure layers	Thickness (cm)	Modulus (MPa)	Poisson's ratio		
AC-13 surface	30	Prony series	0.35		
Base	35	435	0.35		
Subbase	20	604	0.35		
Subgrade	-	174	0.40		
Prony series of AC-13 asphalt mixture at different temperatures					
25 °C	τ (s)	0.0001	0.025	0.2038	1.8502	20.2553	∞
	E_i (MPa)	1710	1065	552	235	103	72
45 °C	τ (s)	0.0001	0.0151	0.1118	1.0954	16.0531	∞
	E_i (MPa)	1709	196	91	42	19	33

The tire consisted of five ribs, while the detailed tire configuration has not been measured. Therefore, the tire-pavement contact stress was predicted by the method in Section 4.3. The distribution of contact stress primarily affects the strain near the pavement surface while barely changing the tensile strain at the bottom of surface, so it has limited influence on the purpose of the verification. Besides, the horizontal stiffness of interface between asphalt layer and base is assumed to be 0.25 and 0.2 MPa/mm for 25 and 45 °C, respectively, because the stiffness would decrease with temperature. These stiffness values are selected from the representative values presented in Section 4.5.
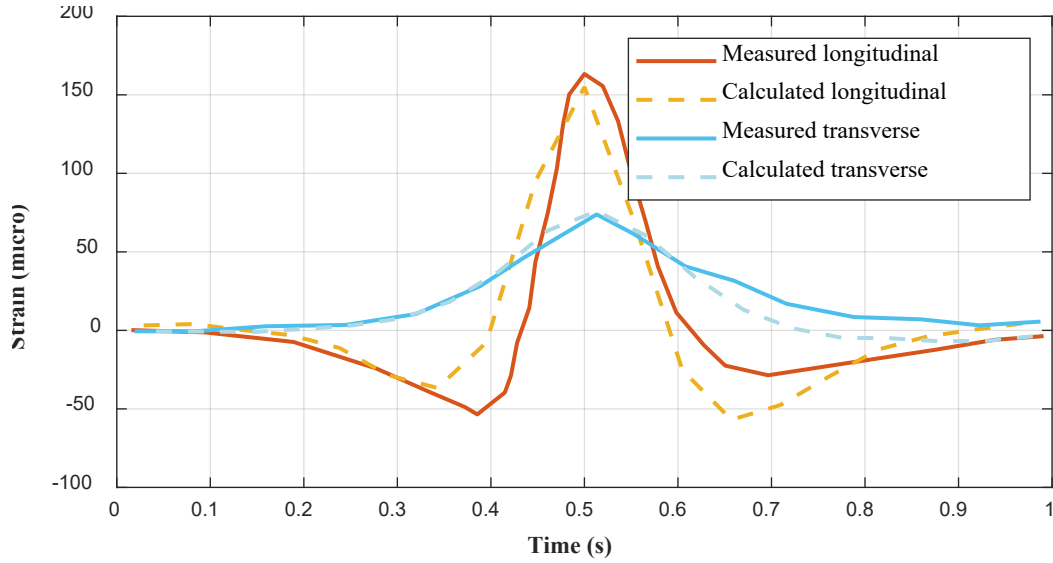
The comparison of the measured [46] and calculated strains at different locations and temperatures is shown in Figure 9, and the trend and extreme value are generally in good agreement. At an intermediate temperature of 25 °C, the asphalt layer is stiffer and can be regarded as a shell supported by base layers. There would be a neutral plane that serves as the boundary between tensile and compressive strains. It can be inferred that the neutral plane is deeper than 6 cm below the surface because the strains at a depth of 6 cm are compressive. As the temperature reaches a high of 45 °C, the asphalt concrete is softening, and the near-surface area will undergo greater deformation. The neutral plane moves upward significantly, and the tensile strain will first increase and then decrease with depth [45].
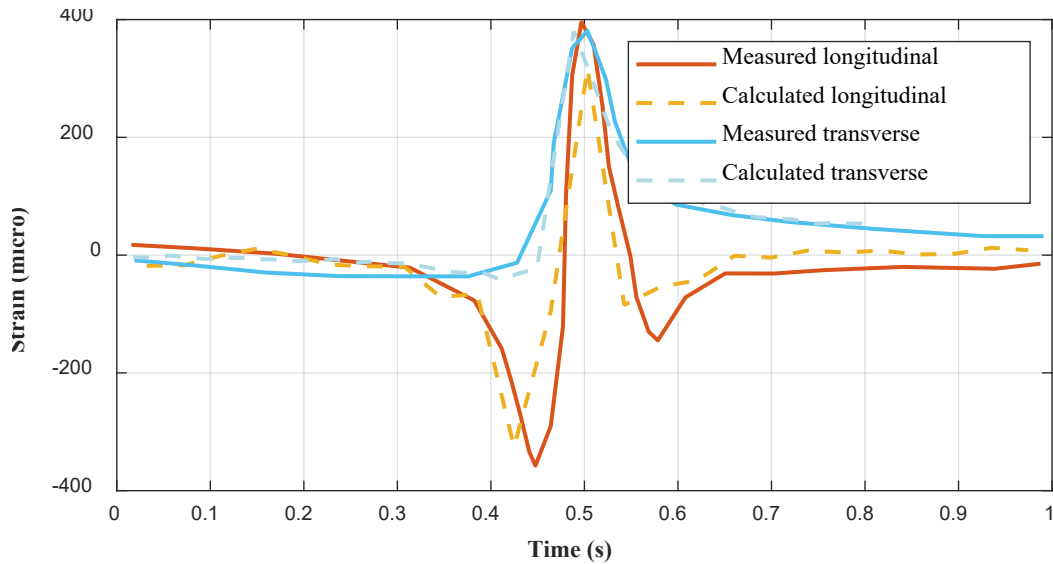
440
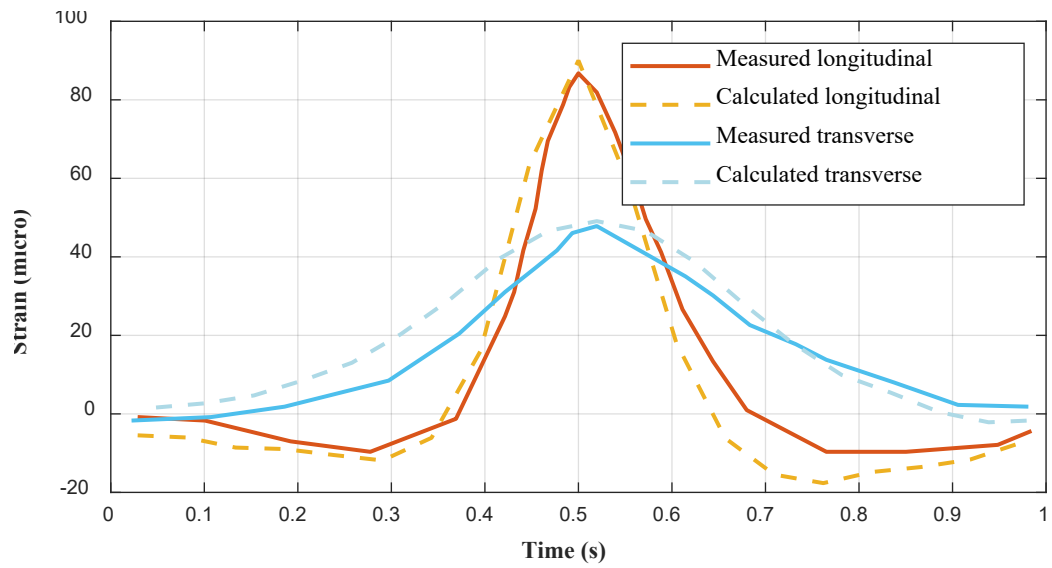
441   (a) Location below surface 30 cm with a temperature of 25 ℃

442
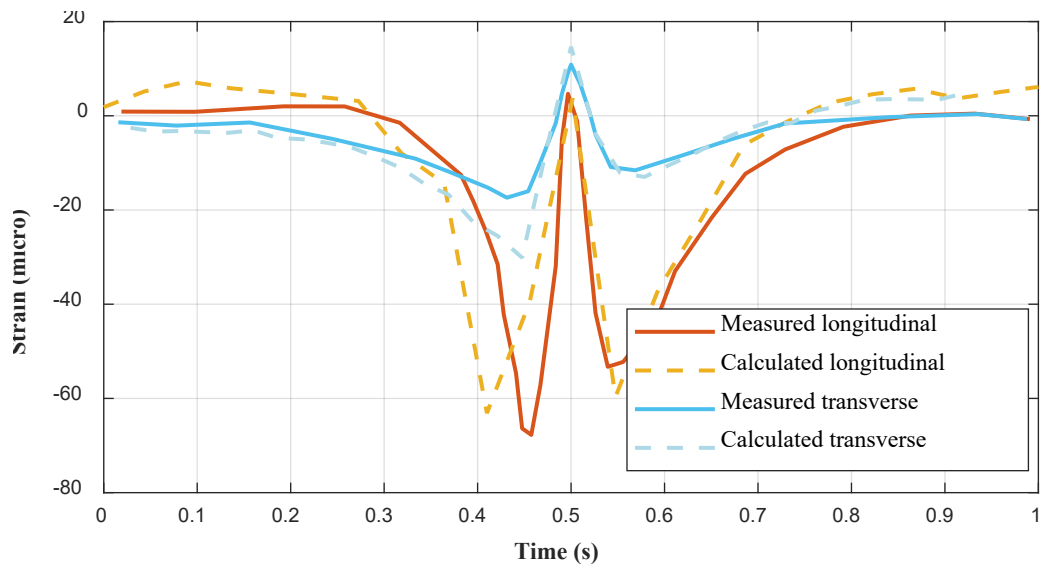
443   (b) Location below surface 6 cm with a temperature of 25 ℃

444

445 (c) Location below surface 30 cm with a temperature of 45 ℃

446

447 (d) Location below surface 6 cm with a temperature of 45 ℃
448 Figure 9. Comparison of measured and calculated strains at different locations and
449 temperatures.

450

451   The relative error between the measured and calculated extreme value of responses
452 is listed in Table 2. It can be found that the relative error of calculated and measured
453 strains at locations 30 cm below the surface is better than that at 6 cm below the surface.
454 There are two potential reasons for the phenomenon. First, the closer to the road surface,
455 the more the structural influence of the strain gauges becomes apparent, which is not
456 accounted for in the simulation model. Second, the impact of the tire-pavement contact
457 stress distribution on pavement responses is more significant closer to the road surface.
458 Since the actual contact stress distribution was not provided, this could lead to
459 discrepancies in the simulation results of near-surface areas.

21

Table 2. Comparison of extreme response value under different conditions.

Location	Temperature (°C)	Measured strain (micro)		Calculated strain (micro)		Relative error (%)	
		L	T	L	T	L	T
6 cm	25	4.7	10.9	3.7	14.7	20.6	34.9
	45	395.6	381.0	317.2	380.3	19.8	0.2
30 cm	25	86.8	47.8	90.0	49.1	3.8	2.6
	45	163.3	73.8	155.0	75.9	5.1	2.8

5.2 Accuracy Validation by Comparison with Field Measurements

The software accuracy is further validated by comparing the computation results with field measurements. An instrumented pavement section (LTPP section 390108 in Ohio) in the long-term pavement performance program (LTPP) database is used [48]. The pavement structure consists of five layers, including asphalt wearing course, asphalt binder course, asphalt-treated base, unbounded aggregate base, and subgrade. The wearing and binder course are treated as a viscoelastic material, while the others are treated as elastic materials.

To measure pavement responses, longitudinal strain gauges were embedded at the bottom of binder course, and pressure cells were installed at the top of subgrade. Besides, the linear variable differential transformers (LVDT) were assembled between the bottom of unbound base and the top of wearing course. Five running tests of a Class 6 truck with a speed of 47 km/h were conducted within one hour at 11 a.m. on August 6, 1996. The rear tandem axle of the truck has a weight of 189 kN, which was assembled with dual tire assembly of 10R22 tire with an inflation pressure of 0.724 MPa. Each tire consists of five ribs with widths of 33, 31, 32, 31, and 33 mm, respectively, and the groove has a width of 8.1 mm. The distance between the center of two tires is 330 mm, and the wheelbase of dual axles is 1.37m. The pavement surface profile with an overall IRI of 0.9 m/km was used to generate dynamic loading forces using TruckSim, a multi-body vehicle dynamics software. In TruckSim, the equations of motion for a truck system with flexible and rigid bodies connected with dynamic and kinematic components can be generated and solved. The pavement surface temperature and air temperature were 37°C and 23°C, respectively, and the temperature gradient was calculated using the BELLS2 model [26]. The pavement dimension, material properties, and loading configuration are presented in the GUI inputs, as shown in Figure 3.

Simulating the whole pavement profile with a length of 134 m is time-consuming because the number of selected Fourier series in SAFEM will increase with the length of longitudinal dimension. Therefore, the profile was divided into 20 subsections and simulated in the software separately. The simulation of each subsection has computation time of 0.5 seconds with an incremental step of 0.01s. The results of each subsection can be summarized to form the overall responses of whole pavement section. Since the location of sensor for field measurements was not recorded in the LTPP database, 16 locations were selected randomly to calculate the range of pavement

495 responses depending on pavement surface roughness and compared with field
496 measurements. Based on data analysis, the reasonable measurement values and
497 corresponding time were used for comparison.

498   Figure 10 shows the comparison of time-history responses under moving loads as
499 compared to the measurement values, respectively, for longitudinal tensile strain at the
500 bottom of asphalt layer, compressive stress at the top of subgrade, and differential
501 displacement between wearing course and unbound base layer. It can be found that most
502 of field measurements are within the range of simulation results or close to the
503 simulation with relative differences of less than 10%. The discrepancy could be caused
504 by the offset of tire loading on the sensors during testing or the variation of in-situ
505 material properties due to construction variation. Considering the uncertainty of field
506 condition, the physical models show satisfactory accuracy in capturing pavement
507 responses under dynamic vehicle loading and ambient environmental conditions.

508
509   (a)
510

23

511
512

(b)

513
514

(c)
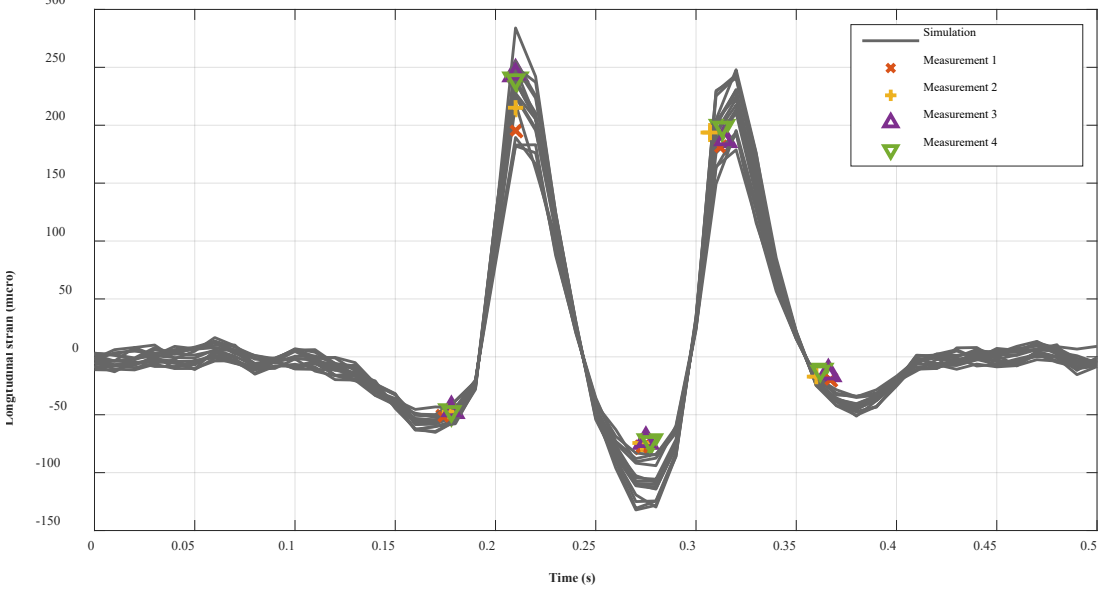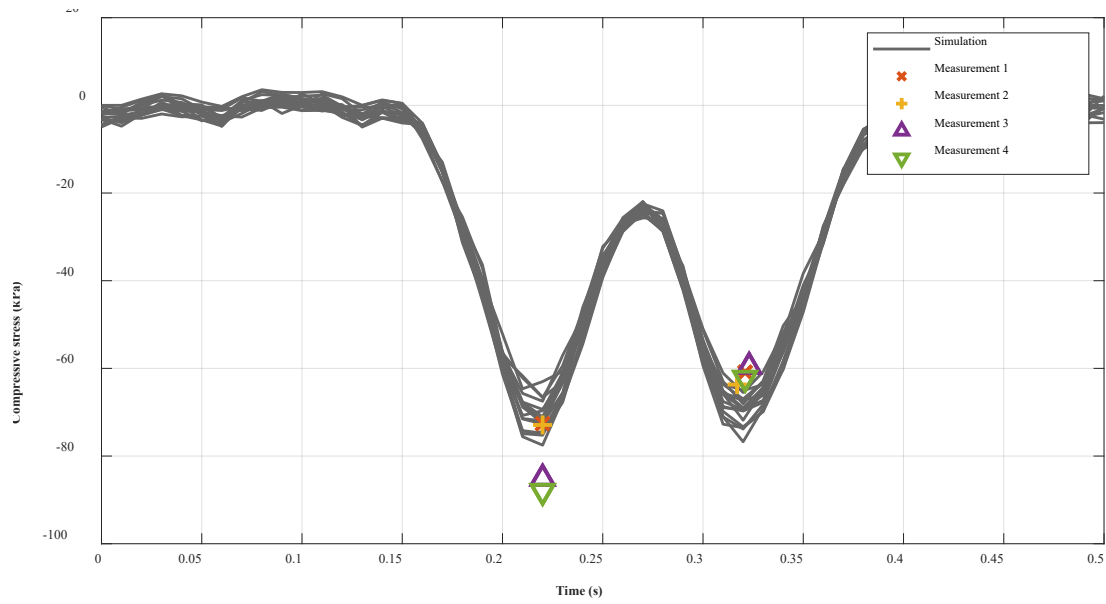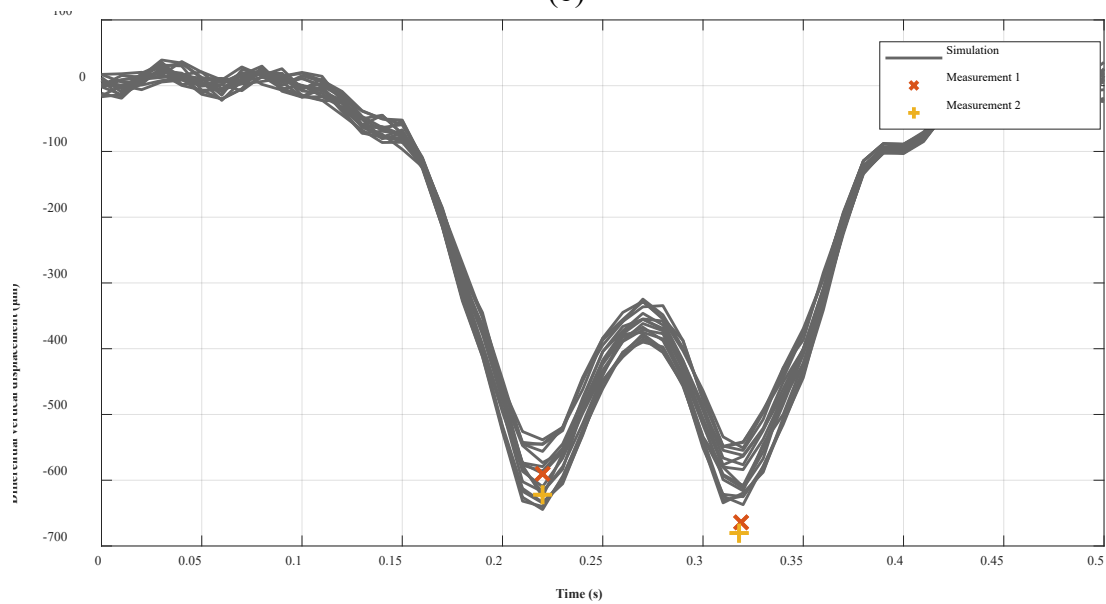
515   Figure 10. Comparison between field measurements and simulation results: (a)
516   longitudinal tensile strain at the bottom of asphalt layer; (b) Compressive stress at the
517   top of subgrade; and (c) Differential displacement between wearing course and
518   unbound base layer.

519

520   **5.3 Efficiency Analysis by Comparison with 3-D FEM**
521   The physical model results from SAFEM_DT and 3-D FEM were compared for
522   efficiency analysis. The pavement model of Section 5.2 is used in the analysis with
523   different model sizes without dynamic loading effect. The 3-D FEM were developed
524   using commercial software ABAQUS.
525   The comparisons of pavement responses under moving tire loading from 3-D FEM
526   and SAFEM are shown in Figure 11, respectively, for longitudinal tensile strain at the

24

527 bottom of asphalt layer, compressive stress on top of subgrade, and surface deflection.
528 The tire loading speed was kept at 20 m/s. Three different longitudinal lengths of
529 pavement models were considered to analyze the impact of model dimensions on
530 pavement responses.
531   The results show that the calculated pavement responses using 3-D FEM,
532 particularly surface deflection, increases with the model length, while those from
533 SAFEM barely change. Comparative analysis suggests that dimension effects diminish
534 over length and reaches stable results as the model length of 3-D reaches 15m, where
535 the pavements responses from SAFEM match well with those from 3-D FEM with
536 relative differences of less than 5%. Therefore, 3-D FEM requires a sufficient length to
537 ensure accuracy, which would increase the model size and accordingly the computation
538 time.

539

540   (a)

541

542

543   (b)
544
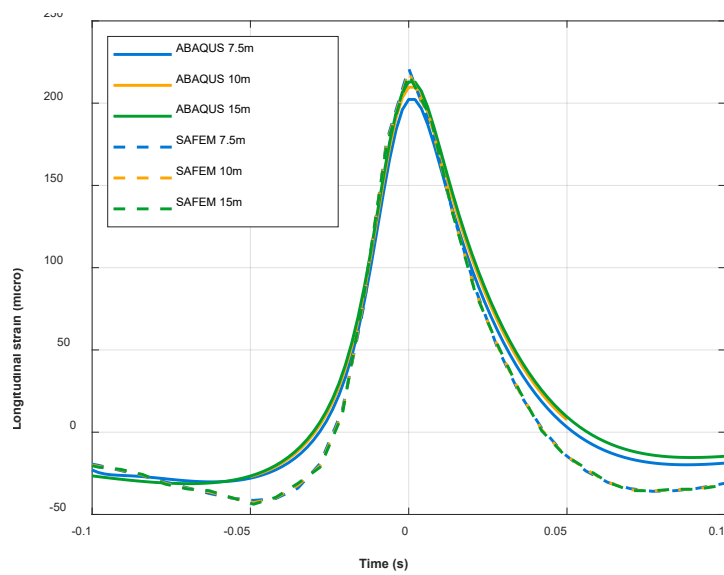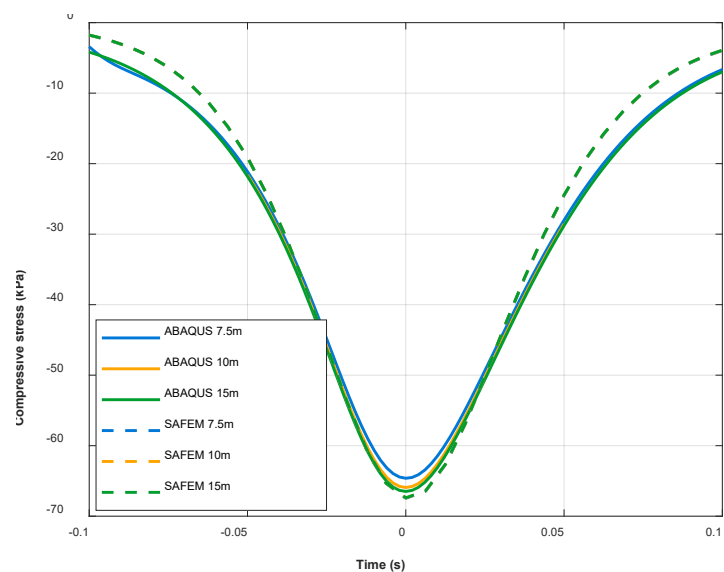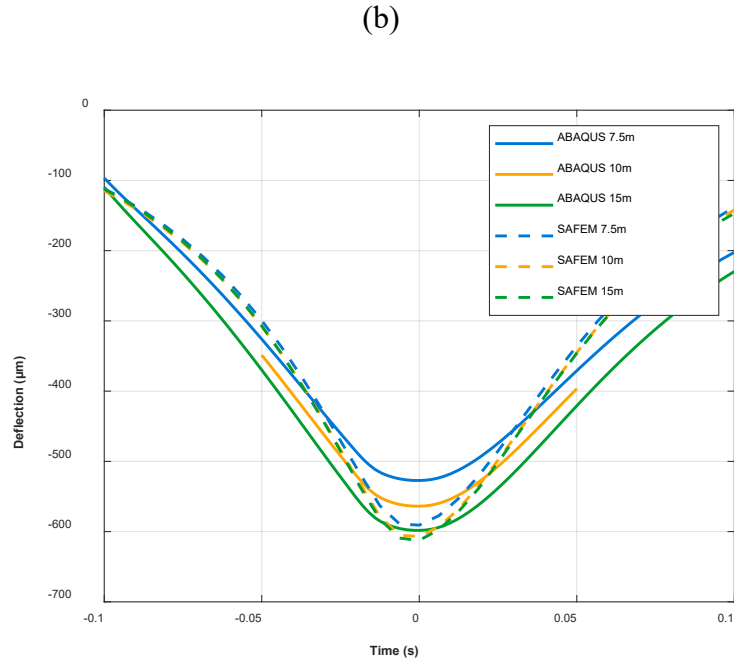
545
546   (c)
547   Figure 11. Comparison of pavement responses between SAFEM and ABAQUS: (a)
548   Longitudinal tensile strain at the bottom of asphalt layer; (b) Compressive stress on
549   top of subgrade; and (c) Surface deflection.
550

551   The computation efficiency of SAFEM_DT, a former SAFEM, and ABAQUS
552   are compared in Table 3. Compared with SAFEM_DT, the former SAFEM does not
553   implement the optimized discrete Fourier transform, GPU acceleration, and sparse
554   matrices while including parallel computing [18]. The analysis results were obtained
555   for the physical model with longitudinal dimension of 10 m and mesh size of 30 mm
556   that is run in the same workstation with a 16-core CPU. Three indicators are used, RAM
557   usage is indicative of computing hardware expenditure, operation time reflects
558   computational efficiency, and output storage corresponds to storage cost implications.
559   The SAFEM_DT with newly implemented algorithms significantly saves RAM usage
560   and operation time. It can also be found that SAFEM_3D shows significant advantages
561   in all aspects compared with the 3-D FEM, saving 99.7%, 90%, and 25% on operation
562   time, storage usage, and hardware usage, respectively.
563
564   Table 3. Computing efficiency of SAFEM and 3D-FEM

	Element Number	Parallel Number	RAM Usage	Operation Time	Output Storage
SAFEM_DT	1,534	54	30 GB	2 mins	0.6 GB
SAFEM	1,534	80	75 GB	15 mins	0.6 GB
3D-FEM	144,480	1	40 GB	11 h	6 GB
Percentage of saving	SAFEM		60%	86.7%	-

26

| 3D-FEM | 25% | 99.7% | 90% |

6 Software Application for Digital Twins of Roadway Infrastructure

The DT of roadway infrastructure is a complex muti-physics system, of which accurate representation requires a combination of multiple simulation models. Strain or stress is the vital indicator to connect the material properties, vehicle-induced responses, and pavement performance evolution. The developed flexible pavement modeling software for DT applications enables fast and responsive computation of pavement responses experienced in the real world, which is further combined with other analysis models to develop the virtual twin of flexible pavement, as shown in Figure 12.
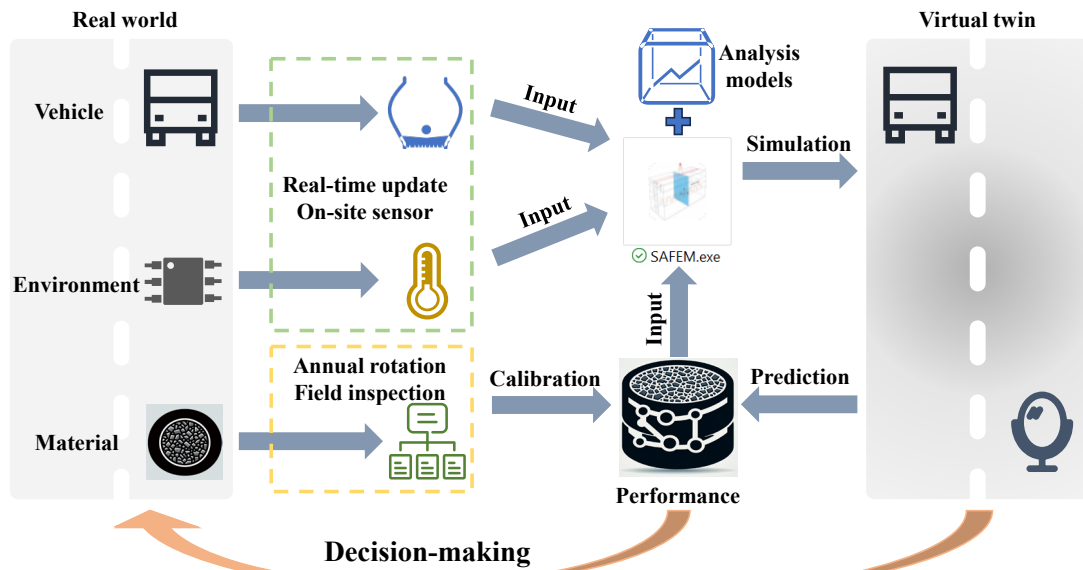

Figure 12. Application of SAFEM_DT for DT of roadway infrastructure

The ability of fast computing makes it possible to incorporate real-time data into its modeling process, such as vehicle dynamics, tire load and pressure, ambient temperature, and in-situ material properties. By inputting the information obtained from on-site measurements of vehicle, pavement, and environment, the software can simulate the stress and strain state experienced in the pavement structure. While vehicle and environmental data can be collected in real time, the acquisition of material property requires data processing and analysis from non-destructive testing that is conducted as periodic inspections by the roadway agency [49]. To accommodate this, the software is designed to update material properties at the end of each simulation cycle. The material property evolution is simulated by other analysis models related to performance prediction, which utilize the strain or stress from the response model as inputs. These updates serve as initial conditions for subsequent cycles, ensuring that the DT continuously represents the current material properties and performance characteristics over different cycles.

A comprehensive digital twin of roadway infrastructure requires the coupling of

593 numerous analysis models. An illustration of the software function within the DT
594 framework is shown by the example of asphalt layer damage caused by vehicle loading.
595 The damage evolution of asphalt layer is usually considered to be related to the micro-
596 cracking induced by energy dissipation [36]. The evolution law can be represented by
597 the viscoelastic continuum damage (VECD) model, which is widely used in damage
598 prediction of flexible pavement [50,51]. The model transforms the convolution of
599 viscoelastic material strain energy into a linear form of pseudo strain. It enables the
600 direct utilization of the stress-strain state of viscoelastic materials to calculate damage
601 accumulation S due to energy dissipation. The pseudo stiffness C, the original stiffness
602 with reduction of damage degree, is further introduced to consider the effect of damage
603 on modulus degradation. The above procedure can be presented with the Figure 13. The
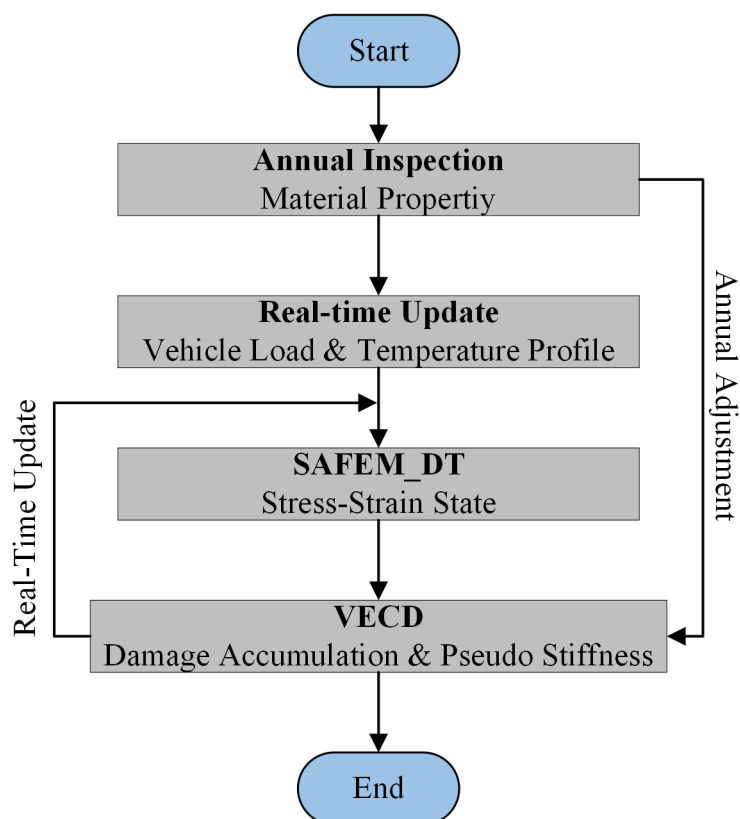604 whole calculation is operated at each element of SAFEM.

605
606 Figure 13. Combination of SAFEM_DT with VECD for damage accumulation.
607

608   The DT requires bidirectional communication between digital information and real
609 infrastructure, and the updating process usually needs to be achieved at different time
610 scales. The vehicle loading and temperature profile can be automatically updated in
611 real-time, while the damage measurement should be completed by annual inspection.
612 This process also highlights the two main characteristics of DT: achieving high-
613 precision virtual twins through bidirectional data exchange and obtaining data that is
614 difficult to acquire in real-time, such as material damage. As more analysis models are
615 integrated, the entire framework can nearly reflect all aspects of the pavement

616   infrastructure, thereby achieving a complete DT of roadway infrastructure.

617

618

619

620   **7 Conclusions and Recommendations**

621 This study developed a high-efficient asphalt pavement modeling software for DT of
622 roadway infrastructure. It is capable of computing viscoelastic pavement responses
623 under moving vehicular loading with dynamic tire forces and realistic tire-pavement
624 contact stresses subject to ambient temperature and different bonding conditions. The
625 software is based on the semi-analytical finite element method, where advanced
626 algorithms and programming are incorporated to enhance efficiency significantly. The
627 crucial parallel computation benefits from the mutually independent characteristics
628 under each Fourier dimension of SAFEM. Moreover, the optimized discrete Fourier
629 transform is also attempted first for such issues. The overall software is developed with
630 object-oriented programming, providing a conducive development environment for
631 subsequent functional expansion and software maintenance.

632   The calculated pavement responses are first verified with a full-scale asphalt
633 pavement test, showing a great relative error below 5% for the tensile strains at the
634 bottom of asphalt layers. The calculated near-surface strain is less accurate, possibly
635 due to the lack of actual tire-pavement contact stress data. Then the calculated results
636 are validated with field measurements of LTPP sections, showing the relative
637 differences of 5-10% due to the variation of in-situ material properties and traffic
638 loading. The SAPAVE_DT shows significant advantage of calculation efficiency as
639 compared with 3-D FEM in terms of operation time, storage usage, and hardware usage.
640 The simulation time of two minutes shows the potential to achieve real-time updates in
641 DT applications.

642   The developed software would lay the groundwork for DT of road infrastructure.
643 Future research is recommended to better characterize material properties considering
644 the effects of asphalt aging and damage for prediction models in the software, such as
645 fatigue cracking and permanent deformation.

646

647   **References**

648 [1]   F. Tao, J. Cheng, Q. Qi, M. Zhang, H. Zhang, F. Sui, Digital twin-driven product
649   design, manufacturing and service with big data, Int. J. Adv. Manuf. Technol. 94
650   (2018) 3563–3576. https://doi.org/10.1007/s00170-017-0233-1.

651 [2]   W.J. Steyn, A. Broekman, Development of a Digital Twin of a Local Road
652   Network: A Case Study, J. Test. Eval. 50 (2022) 20210043.
653   https://doi.org/10.1520/jte20210043.

654 [3]   M. Kaliske, R. Behnke, I. Wollny, Vision on a Digital Twin of the Road-Tire-
655   Vehicle System for Future Mobility, Tire Sci. Technol. 49 (2021) 2–18.
656   https://doi.org/10.2346/tire.21.190223.

657   [4]   C. Han, F. Tang, T. Ma, L. Gu, Z. Tong, Construction quality evaluation of
658   asphalt pavement based on BIM and GIS, Autom. Constr. 141 (2022) 104398.
659   https://doi.org/10.1016/j.autcon.2022.104398.

660   [5]   Y. Pan, L. Zhang, A BIM-data mining integrated digital twin framework for
661   advanced project management, Autom. Constr. 124 (2021) 103564.
662   https://doi.org/10.1016/j.autcon.2021.103564.

663   [6]   C. Han, J. Tong, T. Ma, Z. Tong, S. Wang, Rutting prediction model for semi-
664   rigid base asphalt pavement based on a data-mechanistic dual driven method, Int.
665   J. Pavement Eng. 24 (2023). https://doi.org/10.1080/10298436.2023.2173753.

666   [7]   D. Lee, S.H. Lee, N. Masoud, M.S. Krishnan, V.C. Li, Integrated digital twin
667   and blockchain framework to support accountable information sharing in
668   construction   projects,   Autom.   Constr.   127   (2021)   103688.
669   https://doi.org/10.1016/j.autcon.2021.103688.

670   [8]   AASHTO, Mechanistic-empirical Pavement Design Guide, 2nd ed., American
671   Association of State Highway and Transportation Officials, Washington, D.C.,
672   2015.

673   [9]   J. Fan, T. Ma, J. Zhu, Y. Zhu, Y. Zhang, Characteristics of High-speed deflection
674   basin and structural parameter Back-calculation of asphalt pavement with
675   different structural states, Constr. Build. Mater. 341 (2022) 127869.
676   https://doi.org/10.1016/j.conbuildmat.2022.127869.

677   [10]   K. Shen, H. Wang, Prediction of critical strains of flexible pavement from traffic
678   speed deflectometer measurements, Constr. Build. Mater. 411 (2024) 134770.
679   https://doi.org/10.1016/j.conbuildmat.2023.134770.

680   [11]   S. Erlingsson, A.W. Ahmed, Fast layered elastic response program for the
681   analysis of flexible pavement structures, Road Mater. Pavement Des. 14 (2013)
682   196–210. https://doi.org/10.1080/14680629.2012.757558.

683   [12]   L.A. Myers, R. Roque, B. Birgisson, Use of Two-dimensional Finite Element
684   Analysis to Represent Bending Response of Asphalt Pavement Structures, Int. J.
685   Pavement Eng. 2 (2001) 201–214. https://doi.org/10.1080/10298430108901727.

686   [13]   H. Wang, J. Zhao, X. Hu, X. Zhang, Flexible Pavement Response Analysis under
687   Dynamic Loading at Different Vehicle Speeds and Pavement Surface Roughness
688   Conditions, J. Transp. Eng. Part B Pavements. 146 (2020) 1–10.
689   https://doi.org/10.1061/JPEODX.0000198.

690   [14]   M. Budhu, Soil mechanics and foundations, John Wiley and Sons, 2010.

691   [15]   H. Nasser, A. Chabot, A half-analytical elastic solution for 2D analysis of
692   cracked   pavements,   Adv.   Eng.   Softw.   117   (2018)   107–122.
693   https://doi.org/10.1016/j.advengsoft.2017.06.008.

694   [16]   J. Tong, T. Ma, K. Shen, H. Zhang, S. Wu, A criterion of asphalt pavement
695   rutting based on the thermal-visco-elastic-plastic model, Int. J. Pavement Eng.
696   23 (2022) 1134–1144. https://doi.org/10.1080/10298436.2020.1792470.

697   [17]   K. Shen, H. Zhang, J. Tong, H. Wang, X. Chen, Dynamic elastic analysis of
698   flexible pavements under moving vehicles: a semi-analytical finite element

treatment, Road Mater. Pavement Des. 23 (2022) 1440–1450. https://doi.org/10.1080/14680629.2021.1883467.

[18] K. Shen, H. Wang, H. Zhang, J. Tong, X. Chen, SAPAVE: an improved semi-analytical FE program for dynamic viscoelastic analysis of asphalt pavement, Int. J. Pavement Eng. 23 (2022) 3024–3035. https://doi.org/10.1080/10298436.2021.1878516.

[19] O.C. Zienkiewicz, R.L. Taylor, The finite element method for solid and structural mechanics, Elsevier, 2005.

[20] F.J. Jooste, Flexible pavement response evaluation using the semi-analytical finite element method, Road Mater. Pavement Des. 3 (2002) 211–225. https://doi.org/10.1080/14680629.2002.9689923.

[21] P. Liu, D. Wang, J. Hu, M. Oeser, SAFEM - Software with graphical user interface for fast and accurate finite element analysis of asphalt pavements, J. Test. Eval. 45 (2016) 1301–1315. https://doi.org/10.1520/JTE20150456.

[22] K. Shen, H. Wang, Impact of dynamic loading on pavement deflection measurements from traffic speed deflectometer, Measurement. 217 (2023) 113086. https://doi.org/10.1016/j.measurement.2023.113086.

[23] K. Shen, X. Chen, J. Zhou, H. Zhang, Study of the cement pavement mechanical response using the semi-analytical finite element method, Gongcheng Lixue/Engineering Mech. 37 (2020) 134–144. https://doi.org/10.6052/j.issn.1000-4750.2019.01.0122.

[24] P. Liu, D. Wang, M. Oeser, Application of semi-analytical finite element method to analyze asphalt pavement response under heavy traffic loads, J. Traffic Transp. Eng. (English Ed. 4 (2017) 206–214. https://doi.org/10.1016/j.jtte.2017.03.003.

[25] H. Wang, I.L. Al-Qadi, I. Stanciulescu, Simulation of tyre-pavement interaction for predicting contact stresses at static and various rolling conditions, Int. J. Pavement Eng. 13 (2012) 310–321. https://doi.org/10.1080/10298436.2011.565767.

[26] J. Zhao, H. Wang, D. Ph, M. Asce, Dynamic Pavement Response Analysis under Moving Truck Loads with Random Amplitudes, J. Transp. Eng. Part B Pavements. 146 (2020) 1–9. https://doi.org/10.1061/JPEODX.0000173.

[27] H. Wang, M. Li, N. Garg, Airfield flexible pavement responses under heavy aircraft and high tire pressure loading, Transp. Res. Rec. 2501 (2015) 31–39. https://doi.org/10.3141/2501-05.

[28] J. Tong, K. Shen, T. Ma, J. Zhang, Characterizing the tension-compression asymmetric viscoelasticity of asphalt mixture using the uniaxial tension and compression test, Constr. Build. Mater. 350 (2022) 128854. https://doi.org/10.1016/j.conbuildmat.2022.128854.

[29] H. Wang, M. Li, Evaluation of effects of variations in aggregate base layer properties on flexible pavement performance, Transp. Res. Rec. 2524 (2015) 119–129. https://doi.org/10.3141/2524-12.

[30] H. Ozer, I.L. Al-Qadi, Z. Leng, Fracture-based friction model for pavement

interface characterization, Transp. Res. Rec. (2008) 54–63. https://doi.org/10.3141/2057-07.

[31] H. Ozer, I.L. Al-Qadi, H. Wang, Z. Leng, Characterisation of interface bonding between hot-mix asphalt overlay and concrete pavements: Modelling and in-situ response to accelerated loading, Int. J. Pavement Eng. 13 (2012) 181–196. https://doi.org/10.1080/10298436.2011.596935.

[32] I. Farmaga, P. Shmigelskyi, P. Spiewak, L. Ciupinski, Evaluation of computational complexity of finite element analysis, 2011 11th Int. Conf. - Exp. Des. Appl. CAD Syst. Microelectron. CADSM 2011. (2011) 213–214.

[33] K. Asanovic, R. Bodik, J. Demmel, T. Keaveny, K. Keutzer, J. Kubiatowicz, N. Morgan, D. Patterson, K. Sen, J. Wawrzynek, D. Wessel, K. Yelick, A view of the parallel computing landscape, Commun. ACM. 52 (2009) 56–67. https://doi.org/10.1145/1562764.1562783.

[34] S. Georgescu, P. Chow, H. Okuda, GPU Acceleration for FEM-Based Structural Analysis, Arch. Comput. Methods Eng. 20 (2013) 111–121. https://doi.org/10.1007/s11831-013-9082-8.

[35] A. Abran, J.W. Moore, R. Dupuis, R. Dupuis, L.L. Tripp, Guide to the software engineering body of knowledge, 2001. http://www.mendeley.com/research/guide-software-engineering-body-knowledge-swebok/.

[36] J. Tong, T. Ma, F. Chen, K. Shen, Research of multi-axles effects on the flexible pavement based on the viscoelastic continuum damage model, Road Mater. Pavement Des. 23 (2022) 2765–2780. https://doi.org/10.1080/14680629.2021.1999308.

[37] J.A. Hernandez, A. Gamez, I.L. Al-Qadi, M. De Beer, Analytical approach for predicting three-dimensional tire-pavement contact load, Transp. Res. Rec. 2456 (2014) 75–84. https://doi.org/10.3141/2456-08.

[38] J. Zhao, H. Wang, Dynamic pavement response analysis under wide-base tyre considering vehicle-tyre–pavement interaction, Road Mater. Pavement Des. (2021). https://doi.org/10.1080/14680629.2021.1910551.

[39] J. Zhao, H. Wang, Dynamic Pavement Response Analysis under Moving Truck Loads with Random Amplitudes, J. Transp. Eng. Part B Pavements. 146 (2020) 04020020. https://doi.org/10.1061/jpeodx.0000173.

[40] H. Wang, H. Ozer, I.L. Al-Qadi, C. Armando Duarte, Analysis of near-surface cracking under critical loading conditions using uncracked and cracked pavement models, J. Transp. Eng. 139 (2013) 992–1000. https://doi.org/10.1061/(ASCE)TE.1943-5436.0000562.

[41] H. Wang, I.L. Al-Qadi, Impact quantification of wide-base tire loading on secondary road flexible pavements, J. Transp. Eng. 137 (2011) 630–639. https://doi.org/10.1061/(ASCE)TE.1943-5436.0000245.

[42] G. White, State of the art: interface shear resistance of asphalt surface layers, Int. J. Pavement Eng. 18 (2017) 887–901.

783   https://doi.org/10.1080/10298436.2015.1126270.

784   [43] K. Cook, N. Garg, A. Singh, M. Flynn, Detection of delamination in the HMA
785   layer of runway pavement structure using asphalt strain gauges, J. Transp. Eng.
786   142 (2016). https://doi.org/10.1061/(ASCE)TE.1943-5436.0000869.

787   [44] L. Mohammad, M. Hassan, N. Patel, Effects of shear bond characteristics of tack
788   coats on pavement performance at the interface, Transp. Res. Rec. (2011) 1–8.
789   https://doi.org/10.3141/2209-01.

790   [45] S. Yang, B. Qi, Z. Cao, S. Zhang, H. Cheng, R. Yang, Comparisons between
791   Asphalt Pavement Responses under Vehicular Loading and FWD Loading, Adv.
792   Mater. Sci. Eng. 2020 (2020). https://doi.org/10.1155/2020/5269652.

793   [46] H. Cheng, others, Determination of the stiffness moduli and fatigue endurance
794   limits of asphalt pavements for perpetual pavement design, (2022).

795   [47] H. Cheng, Y. Wang, L. Liu, L. Sun, Effects of using different dynamic moduli
796   on predicted asphalt pavement responses in mechanistic pavement design, Road
797   Mater.   Pavement   Des.   23   (2022)   1860–1876.
798   https://doi.org/10.1080/14680629.2021.1924842.

799   [48] M. Agurla, S. Lin, Long-Term Pavement Performance Ohio SPS-1 and SPS-2
800   Dynamic Load Response Data Processing, McLean, 2015.

801   [49] G.R. Rada, S. Nazarian, B.A. Visintine, R. Siddharthan, S. Thyagarajan,
802   Pavement Structural Evaluation at the Network Level: Final Report, 2016.
803   http://www.ntis.gov.

804   [50] B.S. Underwood, C. Baek, Y.R. Kim, Simplified Viscoelastic Continuum
805   Damage Model as Platform for Asphalt Concrete Fatigue Analysis, Transp. Res.
806   Rec. J. Transp. Res. Board. 2296 (2013) 36–45. https://doi.org/10.3141/2296-04.

807   [51] B.S. Underwood, Y.R. Kim, M.N. Guddati, Improved calculation method of
808   damage parameter in viscoelastic continuum damage model, Int. J. Pavement
809   Eng. 11 (2010) 459–476. https://doi.org/10.1080/10298430903398088.

810